remote sensing

MDPI

Article

Comparison of Land Use Land Cover Classifiers Using Different Satellite Imagery and Machine Learning Techniques

Sana Basheer [1,2], Xiuquan Wang [1,2,*], Aitazaz A. Farooque [1,2], Rana Ali Nawaz [1,2], Kai Liu [3], Toyin Adekanmbi [1,2] and Suqi Liu [1,4]

[1] Canadian Centre for Climate Change and Adaptation, University of Prince Edward Island, St. Peter's Bay, PE C0A 2A0, Canada
[2] School of Climate Change and Adaptation, University of Prince Edward Island, Charlottetown, PE C1A 4P3, Canada
[3] School of Mathematical and Computational Sciences, University of Prince Edward Island, Charlottetown, PE C1A 4P3, Canada
[4] Department of Agriculture and Land, Government of Prince Edward Island, Charlottetown, PE C1A 4N6, Canada
* Correspondence: xxwang@upei.ca

Abstract: Accurate land use land cover (LULC) classification is vital for the sustainable management of natural resources and to learn how the landscape is changing due to climate. For accurate and efficient LULC classification, high-quality datasets and robust classification methods are required. With the increasing availability of satellite data, geospatial analysis tools, and classification methods, it is essential to systematically assess the performance of different combinations of satellite data and classification methods to help select the best approach for LULC classification. Therefore, this study aims to evaluate the LULC classification performance of two commonly used platforms (i.e., ArcGIS Pro and Google Earth Engine) with different satellite datasets (i.e., Landsat, Sentinel, and Planet) through a case study for the city of Charlottetown in Canada. Specifically, three classifiers in ArcGIS Pro, including support vector machine (SVM), maximum likelihood (ML), and random forest/random tree (RF/RT), are utilized to develop LULC maps over the period of 2017–2021. Whereas four classifiers in Google Earth Engine, including SVM, RF/RT, minimum distance (MD), and classification and regression tree (CART), are used to develop LULC maps for the same period. To identify the most efficient and accurate classifier, the overall accuracy and kappa coefficient for each classifier is calculated throughout the study period for all combinations of satellite data, classification platforms, and methods. Change detection is then conducted using the best classifier to quantify the LULC changes over the study period. Results show that the SVM classifier in both ArcGIS Pro and Google Earth Engine presents the best performance compared to other classifiers. In particular, the SVM in ArcGIS Pro shows an overall accuracy of 89% with Landsat, 91% with Sentinel, and 94% with Planet. Similarly, in Google Earth Engine, the SVM shows an accuracy of 87% with Landsat 8 and 92% with Sentinel 2. Furthermore, change detection results show that 13.80% and 14.10% of forest areas have been turned into bare land and urban class, respectively, and 3.90% of the land has been converted into the urban area from 2017 to 2021, suggesting the intensive urbanization. The results of this study will provide the scientific basis for selecting the remote sensing classifier and satellite imagery to develop accurate LULC maps.

Keywords: remote sensing; LULC classification; ArcGIS Pro; Google Earth Engine; machine learning; change detection

check for updates

Citation: Basheer, S.; Wang, X.; Farooque, A.A.; Nawaz, R.A.; Liu, K.; Adekanmbi, T.; Liu, S. Comparison of Land Use Land Cover Classifiers Using Different Satellite Imagery and Machine Learning Techniques. *Remote Sens.* **2022**, *14*, 4978. https://doi.org/10.3390/rs14194978

Academic Editor: Magaly Koch

Received: 13 September 2022
Accepted: 3 October 2022
Published: 6 October 2022

Publisher's Note: MDPI stays neutral with regard to jurisdictional claims in published maps and institutional affiliations.

Copyright: © 2022 by the authors. Licensee MDPI, Basel, Switzerland. This article is an open access article distributed under the terms and conditions of the Creative Commons Attribution (CC BY) license (https://creativecommons.org/licenses/by/4.0/).

1. Introduction

Accurate information on land use land cover (LULC) can facilitate various research activities related to floods, droughts, migration, and climate change at several scales. The constant and precise investigation of LULC is a vital aspect of any region's sustainability

and development. LULC changes (i.e., deforestation and urbanization, etc.) are one the prominent drivers of climate change around the globe [1]. Furthermore, climate change has significant impacts on water balance [2,3], geomorphology [4], water quality and groundwater management [5–8], resources management and their impacts on humans and their surroundings [9], and land monitoring [10–12], all of which require detailed LULC maps as an essential input [13,14]. LULC maps can assist in identifying which types of land are suitable for agriculture practices and watershed management or useful for urban planning. The most frequent method for this purpose is mapping the LULC and analyzing change over time [15–18].

The severity of extreme events is mainly modulated by the LULC changes. The extreme events of heat waves in 2003 and 2010 in Western Europe and Russia inspired researchers to investigate extreme events by looking at the LULC of the area [19–21]. Therefore, it is crucial to identify the best methodology to analyze the change in LULC to address the growing demands of the population to overcome the issues related to agriculture management, natural resource management, and energy generation. Generating more accurate LULC maps for dense regions requires vast quantities of data. As a result, enormous storage capacities, significant computing power, and the ability to employ various strategies are required [22]. Classification of LULC is the foundation of research on LULC change detection. Traditional visual interpretation and mathematical statistics no longer match the criteria for the accuracy of LULC classification [23]. Training samples, classifiers, and supplementary datasets are the most influential components in supervised LULC classification [24]. However, modern state-of-the-art tools (i.e., ArcGIS Pro and Google Earth Engine) enable us to develop more accurate LULC maps using different LULC classification algorithms.

Analysis of different LULC categories, using machine learning approaches, can be performed in a geographic information system platform (i.e., ArcGIS Pro) or Google Earth Engine using remote sensing datasets. The geographic information system can be used for a better understanding of spatial and temporal analysis related to LULC classification [25]. These analyses can help us to understand the trend of change in LULC. Google Earth Engine is a platform that combines remote sensing data (i.e., satellite imagery from different sources) with high-performance computer service, making satellite imagery processing quicker and simple [26–29]. Google Earth Engine contains satellite imagery from various sources, including Landsat 8, Sentinel 2, MODIS, and many other sources of datasets that are freely accessible. JavaScript is used in Google Earth Engine to develop client libraries, while Python handles code modification [30–34]. Google Earth Engine uses the method of MapReduce architecture for parallel processing, which is used for dividing huge volumes of data into smaller sets and proceeding them across several tools. Then, the data were compiled for output datasets after processing them as several individual components.

Recently, state-of-the-art machine learning algorithms (i.e., random forest/random tree (RF/RT), classification and regression tree (CART), support vector machine (SVM), maximum likelihood (ML), and minimum distance (MD)) have captured the researchers' attention [35,36]. Nowadays, most available research focuses on these LULC classifiers comparisons using different machine learning models. Machine learning has the potential to deal with big historical and present datasets using different algorithms for LULC analysis. In the last few decades, many researchers focused on LULC classification using different remote sensing data with machine learning techniques for different types of study areas to analyze the LULC classification at different platforms [24,30,31]. However, only a few studies focus on using the different platforms for LULC classification and mapping, utilizing different LULC classifiers or approaches to compare LULC maps derived from various multispectral satellite images. On the other hand, the stress for accurate LULC data from satellite imagery around the globe increases. Therefore, it is more critical to compare different classification algorithms and their effectiveness in ArcGIS Pro and Google Earth Engine platforms. The objective of this study is to check the performance evaluation of different algorithms or classifiers for LULC categorization utilizing Landsat

8 surface reflectance Tier 1, Sentinel 2 Level-1C, and Planet imagery data with 30 m, 10 m, and 3–5 m resolutions, respectively, with two different platforms (ArcGIS and Google Earth Engine). Moreover, the accuracy of classifiers, i.e., RF/RT, CART, SVM, ML, and MD [37–39] for both platforms, was determined. Furthermore, the changes in LULC for the city of Charlottetown from 2017 to 2021 were also analyzed utilizing the accurate classifier on the selected platform. The results of this study will provide insights for future studies by identifying the most suitable classifier and platform for the remotely sensed images.

2. Data and Methods

2.1. Study Area

This study focuses on Charlottetown, the capital of Prince Edward Island (PEI), commonly known as the Island, a province of Canada located in the Maritimes (Figure 1). PEI has been facing the adverse effects of climate change in the past few decades [40]. Charlottetown is Prince Edward Island's capital. In the past few years, the population of Charlottetown has increased significantly. As a result, the city is facing deforestation and urbanization. The study area has different land cover types (e.g., forest vegetation, water bodies, and urban areas), and its changing due to human interference. Therefore, it is important to analyze the LULC changes with maximum accuracy using the best machine learning approach. Charlottetown has a total size of 44.29 km^2 [41]. It is located on the province's southern coast and has a population of 80,347. Charlottetown is situated on its namesake harbor. By the convergence of three rivers, this harbor was created on the island's south coast. The entrance to the harbor is the Northumberland Strait. The downtown area of Charlottetown consists of the city's five hundred ancient lots and the waterfront area facing the Hillsborough River. Initially, the downtown area was bordered by four villages (Parkdale, Spring Park, Brighton, and Sherwood). The districts to all sides of downtown except the south area have been developed in recent decades with many commercial developments and an increase in residential areas, while the city's outside areas are still primarily farmland.

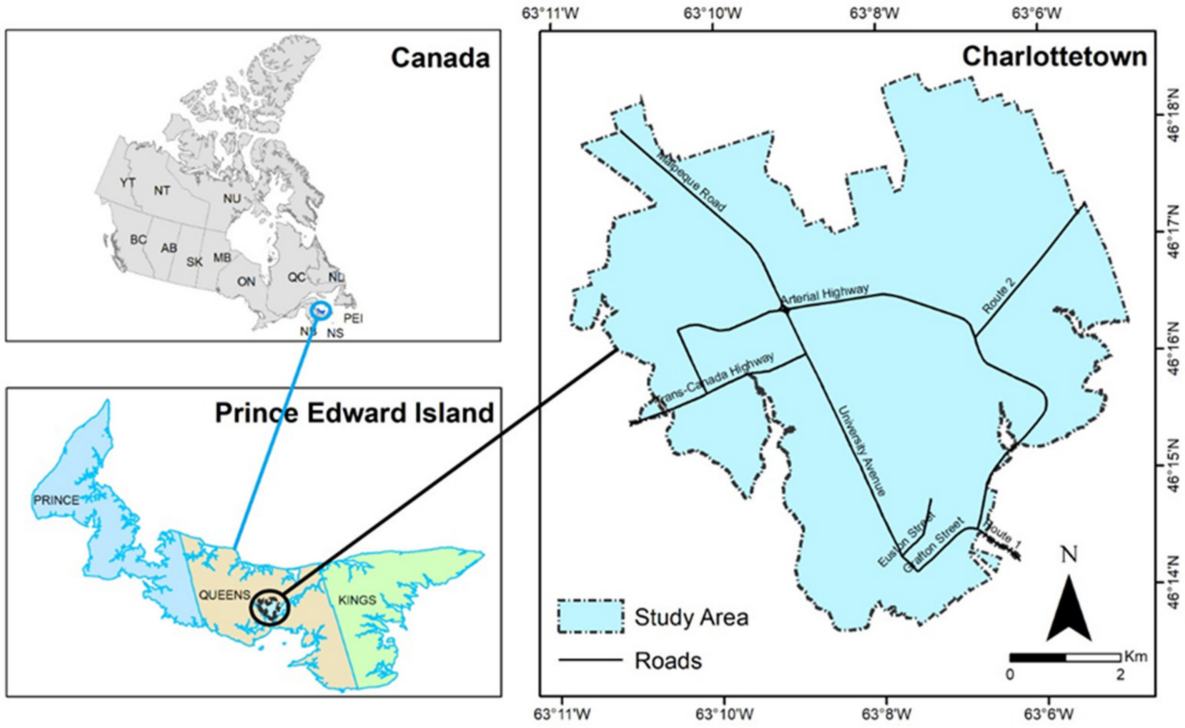


Figure 1. The location of the study area (city of Charlottetown).

2.2. Satellite Data

This project will employ three types of datasets to perform LULC categorization. These datasets include low (Landsat 8), median (Sentinel 2), and high (Planet) resolution satellite images. In this research, all visible and infrared bands (the thermal infrared band was excluded) were used for the LULC analysis [42].

- Landsat 8: the Landsat program is a component of the USGS National Land Imaging (NLI) Program, which has ensured continuity, reliability, and comparability of data since 1974. Landsat has a spatial resolution of 30 m [43].
- Sentinel 2: Sentinel 2 is a high-resolution (10 m), wide-swath, and multispectral imaging system. This aids Copernicus land monitoring studies, such as the examination of water cover and water bodies, vegetation, soil, and the observation related to coastal areas and inland water cover. Sentinel 2 contains thirteen spectral bands [44].
- Planet: since 2016, Planet has captured multispectral photography for consumer use. Planet imagery has high-resolution (3–5 m) imagery that is becoming an essential resource for earth imaging [45]. Planet Scope has more than 150 nanosatellites with a unique combination (coverage of the area, frequency, and high resolution) that can take daily images at a 3 m resolution [25]. These datasets are much more helpful for a better understanding of LULC changes.

2.3. Methodological Framework for LULC Classification

Currently, geospatial Big Data are garnering an abundance of attention and are emphasized globally. ArcGIS Pro and Google Earth Engine are the most popular platforms for large data processing and LULC classification. Several approaches have been established and employed to measure changes in different LULC changes. However, there is currently no research that uses both platforms and includes different input datasets to examine the accurate LULC changes through time in Charlottetown, PEI. In this study, a framework was developed to compare and analyze the performance and viability of different classification methods in ArcGIS Pro and Google Earth Engine, using different datasets. Table 1 shows the major LULC classes scheme for the study area. We use five major classes, e.g., water bodies, urban, forest, bare land, and vegetation, that represent the overall land cover of the city of Charlottetown. Figure 2 shows the methodological frameworks for LULC classification using different classifiers (see Section 2.4) in ArcGIS Pro and Google Earth Engine using Landsat 8, Sentinel 2, and Planet imagery from 2017 to 2021. Image treatment is entirely independent in ArcGIS Pro than in Google Earth Engine. Some data processing factors can affect the outputs, including the algorithms for image selection, cloud masking, and filling the missing pixels. Overall accuracy and kappa coefficient were also calculated to evaluate the performance of each classifier with different input datasets. Maps and graphs were used to display the entire analysis.

Table 1. Name and description of LULC classes scheme.

Class Name	Description of Class
Water Bodies	Lakes, bays, oceans, and estuaries.
Urban	Residential, commercial, industrial, roads and transportation, communications, and utilities.
Forest	Deciduous forest area, evergreen forest, mixed forest, residential forest.
Bare Land	Beaches, sandy areas, open fields without vegetation, exposed rock, gravel pits, transitional areas, and mixed barren land.
Vegetation	Cropland, shrubland, grass.

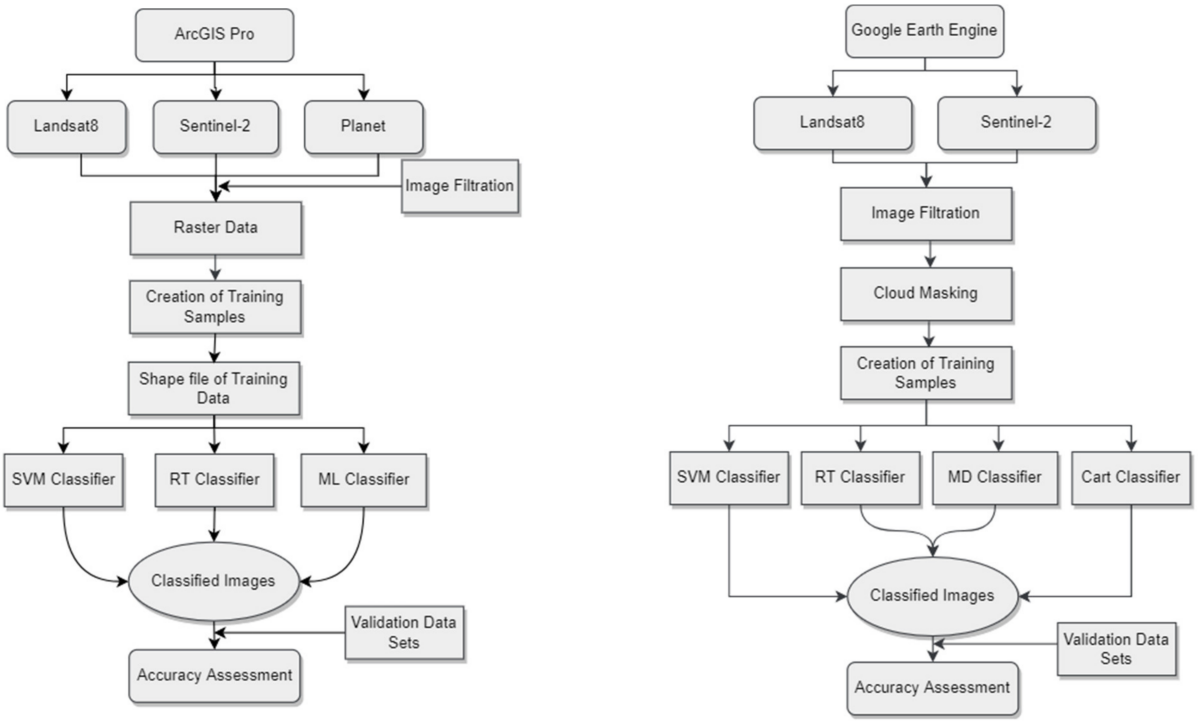


Figure 2. Methodology of LULC classification using (**a**) ArcGIS Pro and (**b**) Google Earth Engine.

2.4. Classification Methods

To perform a pixel-based supervised classification, a set of training samples specific to each year was obtained. Every training sample pixel was assigned to a LULC class on the basis of supplementary data, such as Google Street View and orthophoto images from each year of the study [46]. We use SVM, ML, and RT classier in ArcGIS Pro and CART, SVM, RF, and MD classifiers in the Google Earth Engine platform. In this study, the following classifiers were used for LULC classification:

- Classification and regression tree (CART) is a decision classification tree that facilitates straightforward decision-making and regression analyses [47]. Based on a predetermined threshold, CART runs by separating nodes until it reaches the terminal nodes. This method divides input data into further group sets, and trees are generated using all but one of those group sets. The "classifier.smileCart" approach, which is part of the Google Earth Engine library, was used in this project.
- Random forest/random tree (RF/RT) RF/RT constructs an ensemble classifier and is one of the commonly used classifiers [48] by mixing many CART. RF/RT generates many decision trees using a random selection of training datasets and factors. The two most essential input criteria for this classifier are the size of the training dataset, and the number of trees generated [49,50].
- Support vector machine (SVM). One of the supervised learning techniques is SVM which is used to resolve different problems related to regression and classifications. In the training phase, SVM classifiers generate an ideal hyperplane that splits several classes with the less misclassified pixels from input datasets. The kernel functions, cost parameters, and gamma [51] are key parameters for determining support vectors.
- Minimum distance classifier (MD). The MD classifier classifies imagery datasets into classes that reduce the distance between the class in multi-feature space and image data. This distance between the image data is expressed as a similarity index, such that the minimal distance and highest similarity are equivalent. The main idea behind this process is to calculate the spectral distance between the measurement vector for the candidate pixel and the mean vector for each signature [52].

- Maximum likelihood classifier (ML). Maximum likelihood classifier is a supervised classification method that describes every band by a normal distribution. This supervised classification method is based on the Byes theorem [53].

2.5. Data Processing

In Google Earth Engine, LULC classification maps were generated using Landsat 8 and Sentinel 2 imagery. We use SVM, RF, MD, and CART classifiers in Google Earth Engine. Contaminated pixels caused by cloud cover were eliminated from all images using the cloud mask method provided on the Google Earth Engine [11]. Temporal aggregation approaches such as mean, first, and median was employed to fill the gaps in foggy images.

Using SVM, RT, and ML classifiers, LULC maps were created in ArcGIS Pro. As the major input for classification, images with the least or zero cloud cover were employed. Atmospherically and geometrically corrected images from the three sources (Landsat 8, Sentinel 2, and Planet) with zero cloud cover were utilized as the primary input. The source of data was USGS and Planet Scope sites. Images from the Planet Scope site were mosaiced to cover the whole study area in ArcGIS Pro. Then, all images from all three data sources were clipped to the city of Charlottetown boundary using ArcGIS Pro for LULC classification. Image treatment is entirely independent in ArcGIS Pro than in Google Earth Engine.

A total of 354 training samples were used for LULC classification, from which 284 were used as training samples, and 145 were used as testing samples. Google Earth Pro was used to visually evaluate high-resolution orthophoto images from 2017 to 2021. Training and validation samples were generated with Google Earth Pro. They were then loaded into ArcGIS Pro and the Google Earth Engine platform as shape files to train classifiers. As a rule [54], every classification class should have a minimum of 50 training samples. Training and validation data used for LULC classification was the same in both platforms (ArcGIS Pro and Google Earth Engine). LULC was divided into five broad classes: forest, urban, bare land, water bodies, and vegetation.

For the CART classifier: the optimal cross-validation factor was estimated to be ten based on the research of Kohavi [44] and utilized as an input. For the RT classifier: more trees within the range of 50–100 demonstrated greater classification accuracy and performance [55]. In the present investigation, 100 trees produced positive outcomes. For the SVM classifier: cost, kernel type, and gamma are crucial parameters. The linear kernel is suitable for large datasets [56]. The gamma value is unnecessary for linear kernels. The cost parameter establishes the degree of the punishment for misclassified data, if the C value is greater, it means fewer data misclassifications. For SVM classification, the C-SVC method with a value of 10 as a cost parameter and a linear kernel is also utilized. After LULC classification using post-change detection methodologies, the result of each categorization for the study period was estimated, and a change detection analysis from 2017 to 2021 was also conducted.

2.6. Accuracy Assessment

Methods, procedures, time, and space affected the classification's precision [57–59]. Several research [42,60] found slight to significant variations in the classification accuracy of LULC using different LULC classifiers. The efficacy of various classifiers was evaluated based on their accuracy. The most frequent indicator for measuring the accuracy and also efficiency of all classifiers is overall accuracy, which indicates the percentage of correctly classified testing data. The accuracy evaluation in this investigation reveals a modest discrepancy between the outputs of the classifiers utilized in this instance. The precision of a LULC classification varies not just by classifier but also by location and time. This might be caused by atmospheric, surface, and light fluctuations [61]. Using stratified random sampling, a dataset was generated [62]. Stratified sampling is to divide the dataset or strata according to the characteristics of its attribute. After randomly selecting samples from the types or strata through stratification, these samples in each stratum have a certain

commonality. The main purpose of the stratified sampling method is to obtain the sample data with high efficiency. It is generally believed that stratified sampling makes it easy to extract representative samples [63]. These sampling datasets were separated into validation and training sets. Seventy percent of the entire datasets were used for training, while thirty percent were used as validation datasets [64]. Some auxiliary datasets such as Google Street view were used as a reference to collect the sampling datasets. ArcGIS Pro and Google Earth Engine offer different methods to check the accuracy of many LULC classifiers, and some of these accuracy evaluations were utilized to determine the accuracy of each categorized map from 2017 to 2021.

$$Overall\ Accuracy = \frac{T_{C.P}}{T_{S.P}} \times 100 \quad (1)$$

Whereas $T_{C.P}$ is the total number of correctly classified pixels and $T_{S.P}$ is the total number of sample pixels.

$$kappa\ coefficient = \frac{O.A - C.A}{1 - C.A} \quad (2)$$

Whereas $O.A$ is the overall accuracy and $C.A$ is chance agreement. Equations (1) and (2) show the calculation method of overall accuracy and kappa coefficient. The validation data gathered for each year was compared to each map to generate an error matrix. In addition, the kappa coefficient was determined to evaluate the accuracy of each used classifier for every year throughout the study period in ArcGIS pro and Google Earth Engine platforms for their respective classifiers [65]. We tested all classified results from ArcGIS pro on the ArcGIS Pro platform and tested all Google Earth Engine classified results on the Google Earth Engine platform by the same methods (overall accuracy, kappa coefficient) to check the accuracy. A higher value of the kappa coefficient shows the perfect arrangement of the raster data [66], e.g., 0.8 to 1.0 value shows higher efficiency of LULC classification.

2.7. Change Detection

Numerous techniques exist to identify the LULC change from different imagery datasets [67], but this process is not always convenient or straightforward. Comparing other datasets from different satellites obtained on many dates is relatively straightforward yet effective for change detection in the LULC of any area. Some techniques based on this methodology [68,69] calculate descriptive statistics for the vegetation index difference between two different time points. A threshold of the spectral difference is utilized to distinguish between pixels with and without change. In this study, after the classification and accuracy assessment of all three datasets, we choose the dataset and the classifier with the higher value of overall accuracy and also the kappa coefficient value to analyze the change in LULC using ArcGIS Pro. After that, area change in every class throughout the study period was calculated.

3. Results and Discussion

3.1. LULC Classification Maps

3.1.1. LULC Classification of Landsat 8 Imagery in ArcGIS Pro

From Figure 3, we can observe that the LULC classification of Landsat 8 resulted in most of the forest area being misclassified as an urban class or bare land in the years 2020 and 2021 for RT. Vegetation class was misclassified as bare land as water bodies in 2018 for RT. For the SVM classifier, forest and vegetation were misclassified as urban in 2020 to some extent. Vegetation was also misclassified as bare land or forest in 2018 and 2019. For 2020, SVM classified the image well except for bare land and some urban areas. For all Landsat 8 images from all five years, the SVM classifier performed well in comparison to the other two classifiers in terms of overall accuracy. For 2017 and 2019, the ML classifier misclassified vegetation as a forest. This may be because of identical reflectance, the same as forests [65].

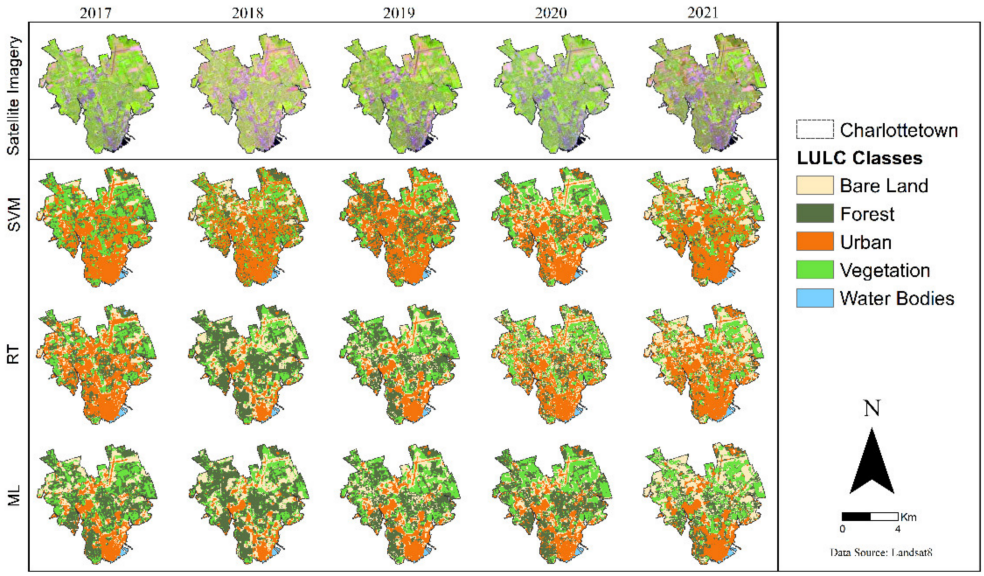


Figure 3. LULC classification maps of Landsat 8 images using SVM, RT, and ML classifiers for the years 2017 to 2021 in ArcGIS Pro.

3.1.2. LULC Classification of Sentinel 2 Imagery in ArcGIS Pro

Figure 4 shows the LULC classification maps using SVM, RT, and ML classifiers for the years 2017 to 2021. From Figure 4, we can see that classification of Sentinel 2 using an SVM classifier resulted in more accuracy as compared to the other two classifiers [11]. For SVM, forest and vegetation were misclassified as urban in 2017 and 2018. For 2021, SVM classified the input imagery data well except for forest and urban classes. For 2020, the RT classifier misclassified the urban and bare land as forest and vegetation in the years 2020 and 2021. Forest was misclassified as urban and, to a lesser extent, as water bodies in 2021 for ML. Vegetation was misclassified as bare land to some extent or forest in 2018 and 2019 using the ML classifier. For 2017 and 2020, the ML classifier misclassified vegetation as bare land and forest, respectively.

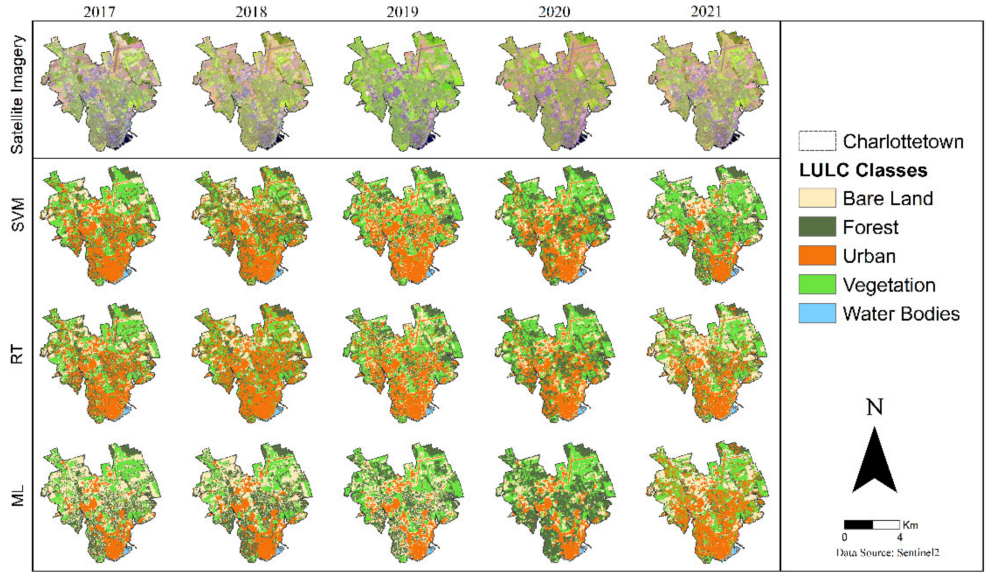


Figure 4. LULC classification maps of Sentinel 2 images using SVM, RT, and ML classifiers for the years 2017 to 2021 in ArcGIS Pro.

3.1.3. LULC Classification of Planet Imagery in ArcGIS Pro

Results show that the classification output of Planet imagery resulted in most of the LULC classes being well classified for the study area with the SVM classifier (Figure 5). For SVM, vegetation was slightly misclassified as bare land and urban in 2020 and 2021. For 2017, the RT classifier misclassified the bare land as vegetation. Forest was misclassified as vegetation and, to some extent, as urban in 2020 and 2021, respectively. For all years, Sentinel 2 images throughout the study period, the ML classifier misclassified the forest and urban areas as bare land in some areas.

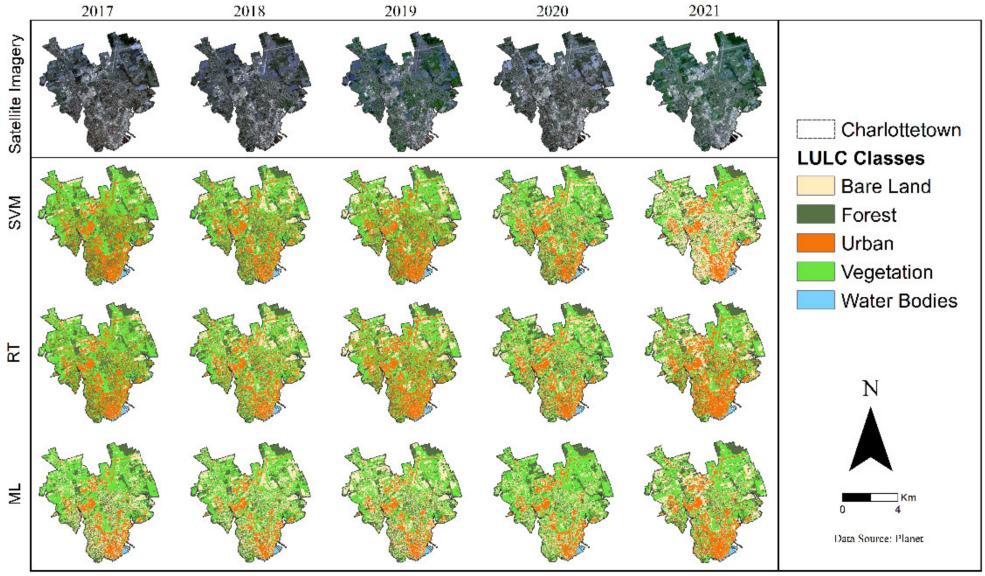


Figure 5. LULC classification maps of Planet images using SVM, RT, and ML classifiers for the years 2017 to 2021 in ArcGIS Pro.

3.1.4. LULC Classification of Landsat 8 Imagery in Google Earth Engine

Figure 6 shows the LULC classification maps using Landsat 8 imagery. In most of the forest area, this class was misclassified as vegetation for the study area with the SVM and CART classifiers in 2020 and 2021. For the SVM classifier, bare land was misclassified as vegetation and urban for 2017 and 2021. For 2017, the RF classifier misclassified the bare land as vegetation. In 2021, vegetation was classified as bare land in some areas. Urban was misclassified as forest in 2017, 2018, and 2019 in the MD classifier. Throughout the study period, the CART classifier misclassified the forest as urban areas. Overall, the SVM classifier performs better than the other three classifiers using Landsat 8 imagery in the Google Earth Engine.

3.1.5. LULC Classification of Sentinel 2 Imagery in Google Earth Engine

Figure 7 shows the classification output of Sentinel 2 imagery, which shows that SVM classifiers perform well as compared to CART, MD, and RF classifiers. For SVM, the forest was misclassified as vegetation and bare land for 2019 and 2020, respectively. For 2017, the RF classifier misclassified the bare land and forest area as urban. In 2020, vegetation was classified as water bodies in some areas. Urban was misclassified as a forest for all five years in the MD classifier [51]. Throughout the study period, the CART classifier misclassified most classes as urban areas [70]. Overall SVM classifier performs better than the other three classifiers as urban and vegetation areas are well classified in the Google Earth Engine using Sentinel 2 imagery.

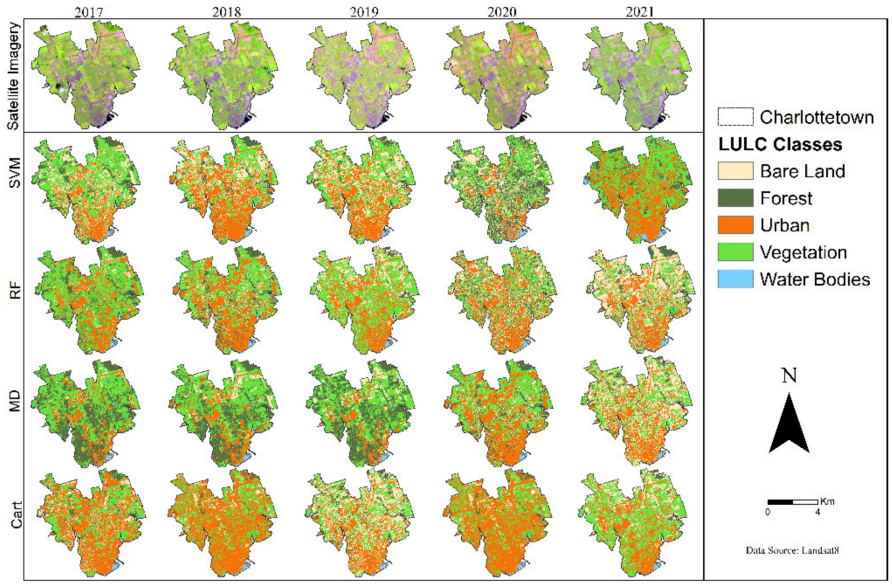


Figure 6. LULC classification maps of Landsat 8 images using SVM, RF, MD, and CART classifiers for the years 2017 to 2021 in Google Earth Engine.

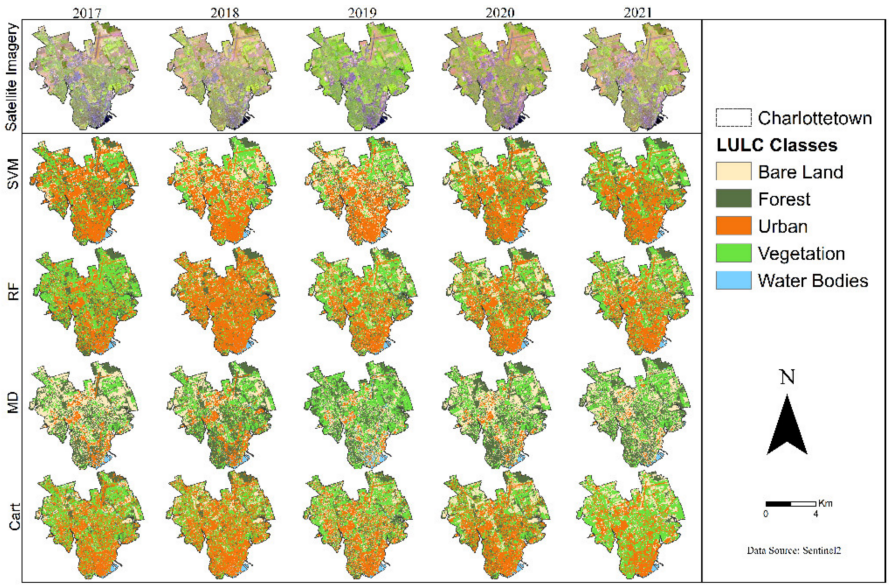


Figure 7. LULC classification maps of Sentinel 2 images using SVM, RF, MD, and CART classifiers for the years 2017 to 2021 in Google Earth Engine.

3.2. Accuracy Assessment

In this research, to check the accuracy of each classifier, we used a validation dataset that was different from the training datasets. By stratified random sampling, we distributed these points over the study area [64] to ensure that all LULC classes accurately and uniformly were represented. After LULC classification using all classifiers, overall accuracy and kappa coefficient were calculated to check the accuracy of these LULC classified maps in the ArcGIS Pro and Google Earth Engine. Tables 2 and 3 show the overall accuracy of different classifiers in ArcGIS Pro and Google Earth Engine platform using Landsat 8, Sentinel 2, and Planet imagery. From Table 2, we can observe the overall accuracy of the SVM classifier with Planet imagery was higher than the other classifiers. The SVM classifier performs higher accuracy with an overall accuracy of 96% in 2017 and 2019 using Planet imagery in ArcGIS Pro. For Sentinel 2 dataset, the higher value of overall accuracy was for the year 2018, with a value of 87%. The lowest value of overall accuracy (74%) for Sentinel

2 imagery was for the year 2019 using the RT classifier. Landsat 8 shows the lowest overall accuracy for all tree classifiers using the ArcGIS Pro platform throughout the study period compared to the other two datasets. Using Landsat 8 imagery, the SVM classifier shows a higher overall accuracy throughout the study period, with the highest value of 85% in 2021.

Table 2. Kappa coefficient and overall accuracy of Landsat 8, Sentinel 2, and Planet imagery for SVM, RT, and ML classifiers using ArcGIS Pro.

Year	Classifier	Landsat 8		Sentinel 2		Planet	
		Overall Accuracy (%)	Kappa Coefficient	Overall Accuracy (%)	Kappa Coefficient	Overall Accuracy (%)	Kappa Coefficient
2017	SVM	84	0.79	86	0.82	96	0.95
	ML	82	0.76	85	0.81	89	0.87
	RT	76	0.72	81	0.75	88	0.85
2018	SVM	83	0.78	87	0.83	90	0.87
	ML	81	0.75	84	0.79	88	0.85
	RT	78	0.71	81	0.77	84	0.84
2019	SVM	80	0.82	85	0.87	96	0.95
	ML	82	0.77	76	0.71	95	0.94
	RT	71	0.65	74	0.67	94	0.92
2020	SVM	83	0.78	84	0.81	94	0.92
	ML	82	0.75	83	0.81	92	0.90
	RT	81	0.72	80	0.77	90	0.87
2021	SVM	85	0.81	86	0.83	93	0.91
	ML	81	0.76	83	0.79	92	0.90
	RT	80	0.73	82	0.77	92	0.90

Table 3. Kappa coefficient and overall accuracy of Landsat 8, Sentinel 2 imagery for SVM, RF, MD, and CART classifiers.

Year	Classifier	Landsat 8		Sentinel 2	
		Overall Accuracy (%)	Kappa Coefficient	Overall Accuracy (%)	Kappa Coefficient
2017	CART	85	0.59	91	0.72
	SVM	88	0.67	92	0.78
	MD	83	0.54	90	0.68
	RF	84	0.55	91	0.73
2018	CART	85	0.64	92	0.80
	SVM	87	0.67	93	0.83
	MD	83	0.53	90	0.68
	RF	84	0.56	91	0.79
2019	CART	88	0.68	91	0.75
	SVM	90	0.80	92	0.82
	MD	86	0.62	89	0.64
	RF	87	0.64	90	0.80
2020	CART	81	0.55	90	0.81
	SVM	83	0.57	92	0.89
	MD	77	0.47	85	0.65
	RF	78	0.49	91	0.83
2021	CART	87	0.70	89	0.72
	SVM	90	0.76	91	0.86
	MD	81	0.64	87	0.74
	RF	85	0.69	88	0.80

Using the Google Earth Engine, the SVM classifier performed the highest overall accuracy of 92% and 90% with Sentinel 2 and Landsat 8 imagery, respectively, in the year 2019 compared with the other three classifiers [71]. In 2021, the MD classifier showed the lowest overall accuracy value, 87%, with Sentinel 2 imagery. Throughout the study, the SVM classifier performs well compared to the other classifiers with Sentinel 2 data. Using Landsat 8 data, the SVM classifier shows the highest overall accuracy of 90% in 2019 and 2021. The lowest overall accuracy of 77% was observed for the MD classifier in 2018. Throughout the study period, the MD classifier showed the lowest overall accuracy with both datasets in the Google Earth Engine platform.

Figure 8a shows the kappa coefficient values for all tested classifiers using three different imagery (Landsat 8, Sentinel 2, and Planet) at the ArcGIS Pro platform. Values of the kappa coefficient from Figure 8a show that Planet imagery shows the highest accuracy with the SVM classifier compared to the other two datasets throughout the study period. Figure 8b shows the values of the kappa coefficient for all tested classifiers using Landsat 8 and Sentinel 2 imagery at the Google Earth Engine platform. The Sentinel 2 dataset shows a higher value of the kappa coefficient as compared to the Landsat 8 dataset from 2017 to 2021 with the SVM classifier. Results show that SVM performs well as compared to CRAT and other classifiers on both platforms. Similar results are reported in the literature [47,72]. At the same time, the lowest value for the kappa coefficient was observed for Landsat 8 data using the RF classifier.

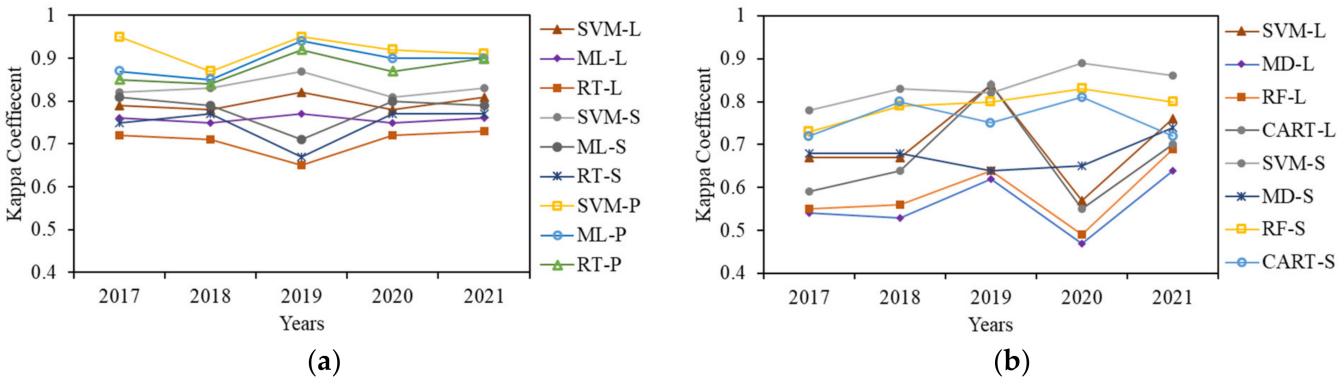


Figure 8. Kappa coefficient (**a**) using SVM, ML, and RT classifiers in ArcGIS Pro, (**b**) using SVM, MD, RF, and CART classifiers in Google Earth Engine.

The average overall accuracy for the SVM, ML, and RT classifiers was 94%, 91%, and 89%, respectively, using Planet imagery. While using Sentinel 2 and Landsat imagery, the overall accuracy for SVM, ML, and RT classifiers was 85%, 82%, 82.2% and 83%, 81%, and 77%, respectively, at the ArcGIS Pro platform. In ArcGIS Pro, the average value of the kappa coefficient from 2017 to 2021 was 0.92 for the SVM classifier using Planet imagery (Table 4), which was higher than the other classifiers. The lowest value for the average kappa coefficient value was observed for the RT classifier using Landsat 8 data, which was 0.70, respectively. In Google Earth Engine, the average value of overall accuracy for the SVM classifier was 0.83 with Sentinel 2 (Table 5), which was higher than the other classifiers for the Sentinel 2 dataset. Using Landsat 8 data, the highest value of average overall accuracy and kappa coefficient with a value of 83% and 0.79 was for the SVM classifier. MD and RF classifiers show almost close values of average overall accuracy and kappa coefficient in the Google Earth Engine platform.

Table 4. Average overall accuracy and average kappa coefficient of Landsat 8, Sentinel 2, and Planet imagery for SVM, RT, and ML classifiers using ArcGIS Pro.

Classifier	Landsat 8		Sentinel 2		Planet	
	Overall Accuracy (%)	Kappa Coefficient	Overall Accuracy (%)	Kappa Coefficient	Overall Accuracy (%)	Kappa Coefficient
SVM	83	0.79	85	0.83	94	0.92
ML	81	0.75	82	0.78	91	0.89
RT	77	0.70	79	0.74	89	0.87

Table 5. Average overall accuracy and average kappa coefficient of Landsat 8, Sentinel 2 imagery for SVM, RF, MD, and CART classifiers using Google Earth Engine.

Classifier	Landsat 8		Sentinel 2	
	Overall Accuracy (%)	Kappa Coefficient	Overall Accuracy (%)	Kappa Coefficient
CART	83	0.63	90	0.76
SVM	87	0.69	92	0.83
MD	84	0.56	88	0.68
RF	82	0.56	89	0.79

3.3. Change Detection

There are a variety of approaches for detecting LULC changes using different satellite image data [68], but this process is not always simple. Comparing remotely sensed data obtained on multiple dates is a simple yet efficient method for change detection [73]. Figure 9 shows the significant changes in the LULC of Charlottetown from 2017 to 2021 in all LULC classes in the city of Charlottetown. A significant change was observed in forest and vegetation classes, which were converted into other LULC classes during the study period. Bare land areas were also converted to urban areas due to rapid urbanization in the study area.

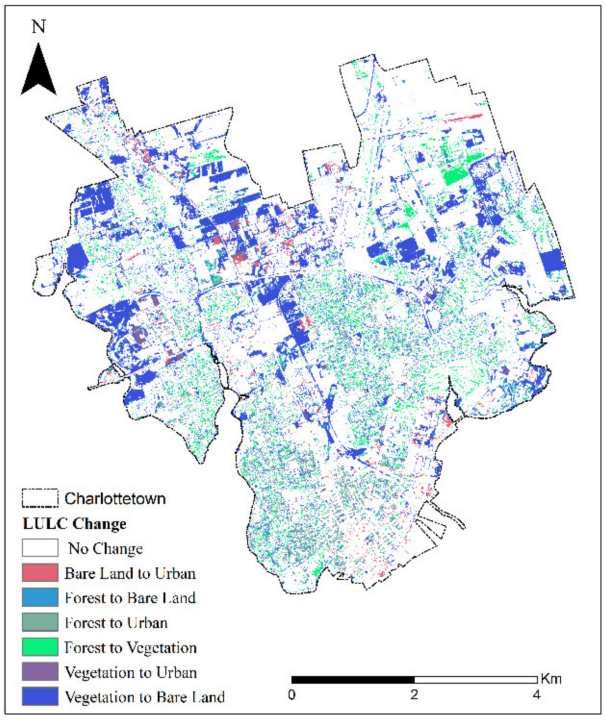


Figure 9. Change in LULC over study area from 2017 to 2019.

The LULC changes can also be determined by using a transition matrix. The transition matrix can explain the change in every LULC class over a specific period [74]. This matrix describes the changed and unchanged amount of area of each LULC class [75]. Change in every class can be observed by a transition matrix in Table 6 from 2017 to 2021 in percentage and km^2. The bare land class changed to the urban class with an increase of 38.81%, showing an urban area expansion from bare land, forest, and vegetation areas as per the literature review. At the same time, another significant change was observed in the vegetation class, which had a decrease of 32.24% in the bare land class and 1.63% in the urban class. Overall, 3.9% of the total study area was converted to an urban area from 2017 to 2021, which shows rapid urbanization in the study area. Forest areas changed into vegetation by 21.3%. Forest area was also converted into bare land by 13.80% due to growth in the lumber industry and into urban by 14.10%, whereas the urban class and water bodies class shows minor changes in their respective area of interest.

Table 6. Transition matrix for area change in different LULC classes from 2017 to 2021 in km^2.

	Bare Land	Forest	Urban	Vegetation	Water Bodies	Area Changes	Area Unchanged	Total Area
Bare Land	0.15	0.33	1.25	0.49	0.00	+2.07	1.15	3.22
	4.65%	10.24%	38.81%	15.21%	0%			
Forest	1.38	5.18	1.41	2.13	0.00	−4.92	5.18	10.10
	13.80%	51.80%	14.10%	21.30%	0%			
Urban	1.29	0.24	9.00	0.014	0.00	+1.54	9.00	10.54
	12.23%	2.29%	86.12%	0.13%	0%			
Vegetation	7.50	0.59	0.33	11.74	0.00	−7.42	12.74	20.16
	37.20%	7.80%	1.63%	58.23%	0%			
Water Bodies	0.01	0.00	0.01	0.00	0.44	−0.011	0.44	0.46
	1.08%	0%	1.30%	0%	95.65%			

4. Conclusions

The climate around the globe has been modified by human activities through the LULC changes. The LULC changes (i.e., deforestation, urbanization, etc.) played an important role in climate change since the pre-industrial era [76]. There are many studies conducted to measure the LULC changes. However, there is no study, to the best of the authors' knowledge, which compares the performance of different approaches available on other platforms. In this study, the performance of different classifiers was observed on two different platforms (ArcGIS Pro and Google Earth Engine) using different datasets, e.g., Landsat 8, Sentinel 2, and Planet imagery. This study aimed to identify the best-performing classifier with different input data. To check the accuracy of different classifiers, the accuracy assessment was performed for every classifier using the error matrix and kappa coefficient for all three satellite imageries from 2017 to 2021. The SVM showed higher accuracy as compared to other classifiers within both platforms. The SVM classifier performs the highest overall accuracy using the Planet imagery on ArcGIS Pro and using Sentinel 2 imagery in the Google Earth Engine. Due to the high resolution of Planet data, it performs well with an average overall accuracy of 94% compared to Sentinel 2 with 85% and Landsat 8 with 83% in the ArcGIS Pro platform. On the Google Earth Engine platform, the SVM classifier performs well with Sentinel 2 imagery with an average overall accuracy of 92% compared to Landsat 8 imagery, which shows 87% accuracy. For this type of study area, which includes different LULC types, e.g., the forest, vegetation, urban, and water bodies, the SVM classifier shows promising results [11].

Change detection analysis shows deforestation and rapid urbanization as 18.80% of forest area was converted to bare land, and 38.81% of bare land was converted to urban area throughout the study period. In addition, some classes may be categorized using expert knowledge and supplementary data [46]. The most accurate and suitable classifier

can also affect by the region of interest, number, and quality of training samples. Similarly, identical reflectance of satellite imagery was another limitation for LULC classification. Some pixels in the LULC maps represent different classes after the LULC classification from the training due to the fact that some of the pixels correspond to different spectral responses. These LULC classifications may be modified based on the study area, data, etc. Furthermore, many studies suggested that the different classifiers show different results in different climatic and geographic situations. Therefore, there is a dire need to further explore the LULC classification accuracy by adding more detailed LULC classes and more training samples with high-resolution input datasets.

Author Contributions: Conceptualization, X.W.; Data curation, S.B.; Formal analysis, R.A.N.; Investigation, A.A.F. and K.L.; Project administration, X.W.; Supervision, X.W.; Validation, S.B. and T.A.; Visualization, A.A.F., R.A.N. and S.L.; Writing—original draft, S.B.; Writing—review and editing, R.A.N., K.L. and T.A. All authors have read and agreed to the published version of the manuscript.

Funding: This research was supported by the Natural Science and Engineering Research Council of Canada, the New Frontiers in Research Fund, Atlantic Canada Opportunities Agency, and Agriculture and Agri-Food Canada.

Data Availability Statement: Publicly available data sets were used in this study. These can be found at: https://earthexplorer.usgs.gov/ (Landsat8 and Sentinel-2 datasets) and https://www.planet.com/explorer/ (Planet datasets).

Conflicts of Interest: The authors declare no conflict of interest.

References

1. Li, Y.; Brando, P.M.; Morton, D.C.; Lawrence, D.M.; Yang, H.; Randerson, J.T. Deforestation-induced climate change reduces carbon storage in remaining tropical forests. *Nat. Commun.* **2022**, *13*, 1964. [CrossRef] [PubMed]
2. Sridhar, V.; Kang, H.; Ali, S.A. Human-Induced Alterations to Land Use and Climate and Their Responses for Hydrology and Water Management in the Mekong River Basin. *Water* **2019**, *11*, 1307. [CrossRef]
3. Sridhar, V.; Jin, X.; Jaksa, W.T.A. Explaining the hydroclimatic variability and change in the Salmon River basin. *Clim. Dyn.* **2012**, *40*, 1921–1937. [CrossRef]
4. Sujatha, E.; Sridhar, V. Spatial Prediction of Erosion Risk of a Small Mountainous Watershed Using RUSLE: A Case-Study of the Palar Sub-Watershed in Kodaikanal, South India. *Water* **2018**, *10*, 1608. [CrossRef]
5. Sridhar, V.; Billah, M.M.; Hildreth, J.W. Coupled Surface and Groundwater Hydrological Modeling in a Changing Climate. *Groundwater* **2017**, *56*, 618–635. [CrossRef] [PubMed]
6. Xiao, Y.; Liu, K.; Yan, H.; Zhou, B.; Huang, X.; Hao, Q.; Zhang, Y.; Zhang, Y.; Liao, X.; Yin, S. Hydrogeochemical constraints on groundwater resource sustainable development in the arid Golmud alluvial fan plain on Tibetan plateau. *Environ. Earth Sci.* **2021**, *80*, 750. [CrossRef]
7. Xiao, Y.; Xiao, D.; Hao, Q.; Liu, K.; Wang, R.; Huang, X.; Liao, X.; Zhang, Y. Accessible Phreatic Groundwater Resources in the Central Shijiazhuang of North China Plain: Perspective From the Hydrogeochemical Constraints. *Front. Environ. Sci.* **2021**, *9*, 475. [CrossRef]
8. Xiao, Y.; Hao, Q.; Zhang, Y.; Zhu, Y.; Yin, S.; Qin, L.; Li, X. Investigating Sources, Driving Forces and Potential Health Risks of Nitrate and Fluoride in Groundwater of a Typical Alluvial Fan Plain. *Sci. Total Environ.* **2022**, *802*, 149909. [CrossRef]
9. Sridhar, V.; Ali, S.A.; Sample, D.J. Systems Analysis of Coupled Natural and Human Processes in the Mekong River Basin. *Hydrology* **2021**, *8*, 140. [CrossRef]
10. Jamali, B.; Bach, P.M.; Cunningham, L.; Deletic, A. A Cellular Automata Fast Flood Evaluation (CA-ffé) Model. *Water Resour. Res.* **2019**, *55*, 4936–4953. [CrossRef]
11. Rahman, A.; Abdullah, H.M.; Tanzir, M.T.; Hossain, M.J.; Khan, B.M.; Miah, M.G.; Islam, I. Performance of Different Machine Learning Algorithms on Satellite Image Classification in Rural and Urban Setup. *Remote Sens. Appl. Soc. Environ.* **2020**, *20*, 100410. [CrossRef]
12. Sridhar, V.; Anderson, K.A. Human-Induced Modifications to Land Surface Fluxes and Their Implications on Water Management under Past and Future Climate Change Conditions. *Agric. For. Meteorol.* **2017**, *234–235*, 66–79. [CrossRef]
13. Cihlar, J. Land Cover Mapping of Large Areas from Satellites: Status and Research Priorities. *Int. J. Remote Sens.* **2000**, *21*, 1093–1114. [CrossRef]
14. Renschler, C.S.; Harbor, J. Soil Erosion Assessment Tools from Point to Regional Scales—The Role of Geomorphologists in Land Management Research and Implementation. *Geomorphology* **2002**, *47*, 189–209. [CrossRef]
15. Roy, D.P.; Wulder, M.A.; Loveland, T.R.; Woodcock, C.E.; Allen, R.G.; Anderson, M.C.; Helder, D.; Irons, J.R.; Johnson, D.M.; Kennedy, R.; et al. Landsat-8: Science and product vision for terrestrial global change research. *Remote Sens. Environ.* **2014**, *145*, 154–172. [CrossRef]

16. Wulder, M.A.; White, J.C.; Loveland, T.R.; Woodcock, C.E.; Belward, A.S.; Cohen, W.B.; Fosnight, E.A.; Shaw, J.; Masek, J.G.; Roy, D.P. The Global Landsat Archive: Status, Consolidation, and Direction. *Remote Sens. Environ.* **2016**, *185*, 271–283. [CrossRef]
17. Gómez, C.; White, J.C.; Wulder, M.A. Optical Remotely Sensed Time Series Data for Land Cover Classification: A Review. *ISPRS J. Photogramm. Remote Sens.* **2016**, *116*, 55–72. [CrossRef]
18. Phan, T.N.; Kuch, V.; Lehnert, L.W. Land Cover Classification Using Google Earth Engine and Random Forest Classifier—The Role of Image Composition. *Remote Sens.* **2020**, *12*, 2411. [CrossRef]
19. Fischer, E.M.; Schär, C. Consistent Geographical Patterns of Changes in High-Impact European Heatwaves. *Nat. Geosci.* **2010**, *3*, 398–403. [CrossRef]
20. Seneviratne, S.I.; Lüthi, D.; Litschi, M.; Schär, C. Land–Atmosphere Coupling and Climate Change in Europe. *Nature* **2006**, *443*, 205–209. [CrossRef]
21. Stott, P.A.; Stone, D.A.; Allen, M.R. Human Contribution to the European Heatwave of 2003. *Nature* **2004**, *432*, 610–614. [CrossRef] [PubMed]
22. Xie, S.; Liu, L.; Zhang, X.; Yang, J.; Chen, X.; Gao, Y. Automatic Land-Cover Mapping Using Landsat Time-Series Data Based on Google Earth Engine. *Remote Sens.* **2019**, *11*, 3023. [CrossRef]
23. Gibril, M.B.A.; Idrees, M.; Yao, K.; Shafri, H.Z.M. Integrative Image Segmentation Optimization and Machine Learning Approach for High Quality Land-Use and Land-Cover Mapping Using Multisource Remote Sensing Data (Erratum). *J. Appl. Remote Sens.* **2018**, *12*, 019902. [CrossRef]
24. Johnson, B. Scale Issues Related to the Accuracy Assessment of Land Use/Land Cover Maps Produced Using Multi-Resolution Data: Comments on "the Improvement of Land Cover Classification by Thermal Remote Sensing". Remote Sens. **2015**, *7*, 8368–8390. *Remote Sens.* **2015**, *7*, 13436–13439. [CrossRef]
25. Szostak, M.; Likus-Cieślik, J.; Pietrzykowski, M. PlanetScope Imageries and LiDAR Point Clouds Processing for Automation Land Cover Mapping and Vegetation Assessment of a Reclaimed Sulfur Mine. *Remote Sens.* **2021**, *13*, 2717. [CrossRef]
26. Gorelick, N.; Hancher, M.; Dixon, M.; Ilyushchenko, S.; Thau, D.; Moore, R. Google Earth Engine: Planetary-Scale Geospatial Analysis for Everyone. *Remote Sens. Environ.* **2017**, *202*, 18–27. [CrossRef]
27. Sidhu, N.; Pebesma, E.; Câmara, G. Using Google Earth Engine to Detect Land Cover Change: Singapore as a Use Case. *Eur. J. Remote Sens.* **2018**, *51*, 486–500. [CrossRef]
28. Tamiminia, H.; Salehi, B.; Mahdianpari, M.; Quackenbush, L.; Adeli, S.; Brisco, B. Google Earth Engine for Geo-Big Data Applications: A Meta-Analysis and Systematic Review. *ISPRS J. Photogramm. Remote Sens.* **2020**, *164*, 152–170. [CrossRef]
29. Kolli, M.K.; Opp, C.; Karthe, D.; Groll, M. Mapping of Major Land-Use Changes in the Kolleru Lake Freshwater Ecosystem by Using Landsat Satellite Images in Google Earth Engine. *Water* **2020**, *12*, 2493. [CrossRef]
30. Shelestov, A.; Lavreniuk, M.; Kussul, N.; Novikov, A.; Skakun, S. Exploring Google Earth Engine Platform for Big Data Processing: Classification of Multi-Temporal Satellite Imagery for Crop Mapping. *Front. Earth Sci.* **2017**, *5*, 17. [CrossRef]
31. Patel, N.N.; Angiuli, E.; Gamba, P.; Gaughan, A.; Lisini, G.; Stevens, F.R.; Tatem, A.J.; Trianni, G. Multitemporal Settlement and Population Mapping from Landsat Using Google Earth Engine. *Int. J. Appl. Earth Obs. Geoinf.* **2015**, *35*, 199–208. [CrossRef]
32. Mateo-García, G.; Gómez-Chova, L.; Amorós-López, J.; Muñoz-Marí, J.; Camps-Valls, G. Multitemporal Cloud Masking in the Google Earth Engine. *Remote Sens.* **2018**, *10*, 1079. [CrossRef]
33. Pimple, U.; Simonetti, D.; Sitthi, A.; Pungkul, S.; Leadprathom, K.; Skupek, H.; Som-ard, J.; Gond, V.; Towprayoon, S. Google Earth Engine Based Three Decadal Landsat Imagery Analysis for Mapping of Mangrove Forests and Its Surroundings in the Trat Province of Thailand. *J. Comput. Commun.* **2018**, *6*, 247–264. [CrossRef]
34. Nery, T.; Sadler, R.; Solis-Aulestia, M.; White, B.; Polyakov, M.; Chalak, M. Comparing Supervised Algorithms in Land Use and Land Cover Classification of a Landsat Time-Series. In Proceedings of the 2016 IEEE International Geoscience and Remote Sensing Symposium (IGARSS), Beijing, China, 10–15 July 2016. [CrossRef]
35. Maxwell, A.E.; Warner, T.A.; Fang, F. Implementation of Machine-Learning Classification in Remote Sensing: An Applied Review. *Int. J. Remote Sens.* **2018**, *39*, 2784–2817. [CrossRef]
36. Adam, E.; Mutanga, O.; Odindi, J.; Abdel-Rahman, E.M. Land-Use/Cover Classification in a Heterogeneous Coastal Landscape Using RapidEye Imagery: Evaluating the Performance of Random Forest and Support Vector Machines Classifiers. *Int. J. Remote Sens.* **2014**, *35*, 3440–3458. [CrossRef]
37. Bar, S.; Parida, B.R.; Pandey, A.C. Landsat-8 and Sentinel-2 Based Forest Fire Burn Area Mapping Using Machine Learning Algorithms on GEE Cloud Platform over Uttarakhand, Western Himalaya. *Remote Sens.Appl. Soc. Environ.* **2020**, *18*, 100324. [CrossRef]
38. Liu, D.; Chen, N.; Zhang, X.; Wang, C.; Du, W. Annual Large-Scale Urban Land Mapping Based on Landsat Time Series in Google Earth Engine and OpenStreetMap Data: A Case Study in the Middle Yangtze River Basin. *ISPRS J. Photogramm. Remote Sens.* **2020**, *159*, 337–351. [CrossRef]
39. Tassi, A.; Vizzari, M. Object-Oriented LULC Classification in Google Earth Engine Combining SNIC, GLCM, and Machine Learning Algorithms. *Remote Sens.* **2020**, *12*, 3776. [CrossRef]
40. *Prince Edward Island (PEI) Climate Change Risk Assessment*; Department of Environment, Energy and Climate Action: Charlottetown, PE, Canada, 2021.
41. Wikipedia Contributors. Charlottetown. Available online: https://en.wikipedia.org/wiki/Charlottetown (accessed on 1 June 2022).

42. Reis, S. Analyzing Land Use/Land Cover Changes Using Remote Sensing and GIS in Rize, North-East Turkey. *Sensors* **2008**, *8*, 6188–6202. [CrossRef]
43. Wahab, N.A.; Shafri, H.Z. *Utilization of Google Earth Engine (GEE) for Land Cover Monitoring over Klang Valley, Malaysia*; IOP Conference Series: Earth and Environmental Science; IOP Publishing: Bristol, UK, 2020; Volume 540, p. 012003.
44. Ustin, S.L.; Middleton, E.M. Current and near-term advances in Earth observation for ecological applications. *Ecol. Process.* **2021**, *10*, 1. [CrossRef]
45. Frazier, A.E.; Hemingway, B.L. A Technical Review of Planet Smallsat Data: Practical Considerations for Processing and Using PlanetScope Imagery. *Remote Sens.* **2021**, *13*, 3930. [CrossRef]
46. Gordon, A.D.; Breiman, L.; Friedman, J.H.; Olshen, R.A.; Stone, C.J. Classification and Regression Trees. *Biometrics* **1984**, *40*, 874. [CrossRef]
47. Shetty, S. Analysis of Machine Learning Classifiers for LULC Classification on Google Earth Engine. Master's Thesis, University of Twente, Enschede, The Netherlands, 2019.
48. Breiman, L. Random Forests. *Mach. Learn.* **2001**, *45*, 5–32. [CrossRef]
49. Xie, Z.; Chen, Y.; Lu, D.; Li, G.; Chen, E. Classification of Land Cover, Forest, and Tree Species Classes with ZiYuan-3 Multispectral and Stereo Data. *Remote Sens.* **2019**, *11*, 164. [CrossRef]
50. Pal, M. Random forest classifier for remote sensing classification. *Int. J. Remote Sens.* **2005**, *26*, 217–222. [CrossRef]
51. Talukdar, S.; Singha, P.; Mahato, S.; Shahfahad; Pal, S.; Liou, Y.-A.; Rahman, A. Land-Use Land-Cover Classification by Machine Learning Classifiers for Satellite Observations—A Review. *Remote Sens.* **2020**, *12*, 1135. [CrossRef]
52. Murtaza, K.O.; Romshoo, S.A. Determining the suitability and accuracy of various statistical algorithms for satellite data classification. *Int. J. Geomat. Geosci.* **2014**, *4*, 585–599.
53. Norovsuren, B.; Tseveen, B.; Batomunkuev, V.; Renchin, T.; Natsagdorj, E.; Yangiv, A.; Mart, Z. Land Cover Classification Using Maximum Likelihood Method (2000 and 2019) at Khandgait Valley in Mongolia. *IOP Conf. Ser. Earth Environ. Sci.* **2019**, *381*, 012054. [CrossRef]
54. Thomas, M.L.; Ralph, W.; Kiefer, J.C. Remote Sensing and Image Interpretation (Fifth Edition). *Geogr. J.* **2004**, *146*, 448–449. [CrossRef]
55. Kohavi, R. *A Study of Cross-Validation and Bootstrap for Accuracy Estimation and Model Selection*; Ijcai: Montreal, QC, Canada, 1995; Volume 14, pp. 1137–1145.
56. Belgiu, M.; Drăguţ, L. Random Forest in Remote Sensing: A Review of Applications and Future Directions. *ISPRS J. Photogramm. Remote Sens.* **2016**, *114*, 24–31. [CrossRef]
57. Hsu, C.W.; Chang, C.C.; Lin, C.J. *A Practical Guide to Support Vector Classification*; Technical Report; Department of Computer Science and Information Engineering, University of National Taiwan: Taipei, Taiwan, 2003; pp. 1396–1400.
58. Camargo, F.F.; Sano, E.E.; Almeida, C.M.; Mura, J.C.; Almeida, T. A Comparative Assessment of Machine-Learning Techniques for Land Use and Land Cover Classification of the Brazilian Tropical Savanna Using ALOS-2/PALSAR-2 Polarimetric Images. *Remote Sens.* **2019**, *11*, 1600. [CrossRef]
59. Rodriguez-Galiano, V.F.; Chica-Rivas, M. Evaluation of Different Machine Learning Methods for Land Cover Mapping of a Mediterranean Area Using Multi-Seasonal Landsat Images and Digital Terrain Models. *Int. J. Digit. Earth* **2012**, *7*, 492–509. [CrossRef]
60. Foody, G.M. Harshness in Image Classification Accuracy Assessment. *Int. J. Remote Sens.* **2008**, *29*, 3137–3158. [CrossRef]
61. Islam, K.; Jashimuddin, M.; Nath, B.; Nath, T.K. Land Use Classification and Change Detection by Using Multi-Temporal Remotely Sensed Imagery: The Case of Chunati Wildlife Sanctuary, Bangladesh. *Egypt. J. Remote Sens. Space Sci.* **2018**, *21*, 37–47. [CrossRef]
62. Manandhar, R.; Odeh, I.; Ancev, T. Improving the Accuracy of Land Use and Land Cover Classification of Landsat Data Using Post-Classification Enhancement. *Remote Sens.* **2009**, *1*, 330–344. [CrossRef]
63. Li, C.; Ma, Z.; Wang, L.; Yu, W.; Tan, D.; Gao, B.; Feng, Q.; Guo, H.; Zhao, Y. Improving the Accuracy of Land Cover Mapping by Distributing Training Samples. *Remote Sens.* **2021**, *13*, 4594. [CrossRef]
64. Zhao, Y.; Gong, P.; Yu, L.; Hu, L.; Li, X.; Li, C.; Zhang, H.; Zheng, Y.; Wang, J.; Zhao, Y.; et al. Towards a common validation sample set for global land-cover mapping. *Int. J. Remote Sens.* **2014**, *35*, 4795–4814. [CrossRef]
65. Loukika, K.N.; Keesara, V.R.; Sridhar, V. Analysis of Land Use and Land Cover Using Machine Learning Algorithms on Google Earth Engine for Munneru River Basin, India. *Sustainability* **2021**, *13*, 13758. [CrossRef]
66. McHugh, M.L. Interrater Reliability: The Kappa Statistic. *Biochem. Med.* **2012**, *22*, 276–282. [CrossRef]
67. Costa, H.; Almeida, D.; Vala, F.; Marcelino, F.; Caetano, M. Land Cover Mapping from Remotely Sensed and Auxiliary Data for Harmonized Official Statistics. *ISPRS Int. J. Geo-Inf.* **2018**, *7*, 157. [CrossRef]
68. Zhu, Z. Change Detection Using Landsat Time Series: A Review of Frequencies, Preprocessing, Algorithms, and Applications. *ISPRS J. Photogramm. Remote Sens.* **2017**, *130*, 370–384. [CrossRef]
69. Lu, D.; Mausel, P.; Brondízio, E.; Moran, E. Change Detection Techniques. *Int. J. Remote Sens.* **2004**, *25*, 2365–2401. [CrossRef]
70. Ramachandra, T.; Kumar, U. Geographic Resources Decision Support System for Land Use, Land Cover Dynamics Analysis. In Proceedings of the FOSS/GRASS Users Conference, Bangkok, Thailand, 12–14 September 2004; pp. 12–14.
71. Pu, R.; Gong, P.; Tian, Y.; Miao, X.; Carruthers, R.I.; Anderson, G.L. Using Classification and NDVI Differencing Methods for Monitoring Sparse Vegetation Coverage: A Case Study of Saltcedar in Nevada, USA. *Int. J. Remote Sens.* **2008**, *29*, 3987–4011. [CrossRef]

72. Shao, Y.; Lunetta, R.S. Comparison of Support Vector Machine, Neural Network, and CART Algorithms for the Land-Cover Classification Using Limited Training Data Points. *ISPRS J. Photogramm. Remote Sens.* **2012**, *70*, 78–87. [CrossRef]
73. Jin, S.; Yang, L.; Danielson, P.; Homer, C.; Fry, J.; Xian, G. A Comprehensive Change Detection Method for Updating the National Land Cover Database to circa 2011. *Remote Sens. Environ.* **2013**, *132*, 159–175. [CrossRef]
74. Shi, G.; Jiang, N.; Yao, L. Land Use and Cover Change during the Rapid Economic Growth Period from 1990 to 2010: A Case Study of Shanghai. *Sustainability* **2018**, *10*, 426. [CrossRef]
75. Hu, Y.; Batunacun; Zhen, L.; Zhuang, D. Assessment of Land-Use and Land-Cover Change in Guangxi, China. *Sci. Rep.* **2019**, *9*, 2189. [CrossRef]
76. Solomon, S.; On, P.; Al, E. *Climate Change 2007: The Physical Science Basis*; Cambridge University Press: Cambridge, UK, 2007.